

Nonlinear Dispersion Relation and Out-of-Plane Second Harmonic Generation in MoSSe and WSSe Janus Monolayers

Marko M. Petrić,^{1,2,*} Viviana Villafañe,^{3,2} Paul Herrmann,⁴ Amine Ben Mhenni,^{3,2} Ying Qin,⁵ Yasir Sayyad,⁵ Yuxia Shen,⁵ Sefaattin Tongay,^{5,†} Kai Müller,^{1,2} Giancarlo Soavi,^{4,6,‡} Jonathan J. Finley,^{3,2} and Matteo Barbone^{1,2,§}

¹Walter Schottky Institut and Department of Electrical and Computer Engineering, Technische Universität München, Am Coulombwall 4, 85748 Garching, Germany

²Munich Center for Quantum Science and Technology (MCQST), Schellingstrasse 4, 80799 Munich, Germany

³Walter Schottky Institut and Physik-Department,

Technische Universität München, Am Coulombwall 4, 85748 Garching, Germany

⁴Institute of Solid State Physics, Friedrich Schiller University Jena, Max-Wien-Platz 1, Jena, 07743 Germany

⁵Materials Science and Engineering, School for Engineering of Matter,

Transport and Energy, Arizona State University, Tempe, Arizona 85287, USA

⁶Abbe Center of Photonics, Friedrich Schiller University Jena, Albert-Einstein-Straße 6, 07745 Jena, Germany

Janus transition metal dichalcogenides are an emerging class of atomically thin materials with engineered broken mirror symmetry that gives rise to long-lived dipolar excitons, Rashba splitting, and topologically protected solitons. They hold great promise as a versatile nonlinear optical platform due to their broadband harmonic generation tunability, ease of integration on photonic structures, and nonlinearities beyond the basal crystal plane. Here, we study second and third harmonic generation in MoSSe and WSSe Janus monolayers. We use polarization-resolved spectroscopy to map the full second-order susceptibility tensor of MoSSe, including its out-of-plane components. In addition, we measure the effective third-order susceptibility, and the second-order nonlinear dispersion close to exciton resonances for both MoSSe and WSSe at room and cryogenic temperatures. Our work sets a bedrock for understanding the nonlinear optical properties of Janus transition metal dichalcogenides and probing their use in the next-generation on-chip multifaceted photonic devices.

Nonlinear optics with atomically thin and layered materials has proven to be a powerful spectroscopic approach to study the physics of excitons confined at the ultimate thickness limit, as well as a fruitful playground to test novel ultrafast and ultrathin optical devices [1]. Parametric harmonic generation has been used to probe interlayer excitons in homo-[2] and hetero-bilayers [3], and to detect quantum interference pathways and strong coupling in monolayer transition metal dichalcogenides (TMDs) [4]. Furthermore, nonlinear optical properties of layered materials are adding a rapidly growing number of applications in optics, which already include electrical [5] and all-optical [6] ultrafast and broadband frequency converters, miniaturized logic gates [7, 8], photonic integrated gas sensors [9], nonlinear holograms [10], and ultrathin quantum sources based on spontaneous parametric down conversion (SPDC) [11].

Lately, a new class has expanded the family of atomically thin materials: Janus transition metal dichalcogenide (Janus TMD) monolayers are van der Waals materials with different chalcogen atoms within the crystal unit cell, which breaks mirror symmetry, and creates an out-of-plane electrical polarity due to charge imbalance [12–14]. The structural mirror-symmetry breaking in Janus TMD monolayers gives rise to physical effects and functionalities beyond those offered by conventional TMDs, such as Rashba spin-splitting [15–20], and topologically-protected and localized solitonic spin textures [21–23]. Moreover, due to the reduced overlap between electron and hole wavefunctions, Janus TMD monolayers host longer-lived dipolar excitons than

mirror-symmetric TMDs [24–27], making them a potential platform for exciton Bose-Einstein condensation and other strongly correlated many-body states [28]. Since their theoretical prediction in 2013 [15] and first synthesis in 2017 [29, 30], a multitude of morphotaxy-based techniques [31] have emerged breaching bottlenecks towards the synthesis of high-quality MoSSe and WSSe Janus monolayers [32–38]. Further studies have already provided insight into their vibrational properties [39, 40], interlayer coupling strength [27, 41, 42], and dipole emission profile [43].

Atomically thin crystals provide two distinct advantages compared to conventional bulk materials used in nonlinear optics. First, a high degree of compatibility with on-chip photonic architectures [44–47]. Second, their atomically thin nature combined with a strong nonlinear response [1, 48] allows for efficient frequency conversion without phase matching constraints [49, 50], and thus, provides a viable route towards ultra-broadband classical and quantum sources of light. Janus TMD monolayers further expand such advantages by respectively adding out-of-plane components in the nonlinear optical response [51–53], which introduce an additional functionality to be harnessed in vertical photonics structures [54, 55], and widening the spectral region of resonantly enhanced nonlinear optics to different areas of the visible and near-infrared light [56]. To capitalize on such advantages, understanding the wavelength-dependent second harmonic generation (SHG) efficiency (*i.e.*, the nonlinear dispersion) and mapping the corresponding susceptibility tensor in Janus TMD monolayers

is essential.

In this work, we address both these open issues and provide a detailed study of the out-of-plane second-order nonlinear susceptibility in MoSSe Janus monolayer, using a simplified approach that fully maps the susceptibility tensor using a high numerical aperture (NA) objective. Furthermore, we measure third harmonic generation (THG) and the wavelength-dependent SHG efficiency of MoSSe and WSSe Janus monolayers, revealing the A and B exciton resonances at room and cryogenic temperatures.

RESULTS AND DISCUSSION

Janus TMD monolayers were fabricated *via* a room temperature selective epitaxy atomic replacement method [33]. In this process, the top-layer selenium atoms in previously grown MoSe₂ (on Si/SiO₂) and WSe₂ (on Al₂O₃) parent monolayers are replaced by sulfur atoms, resulting in MoSSe and WSSe Janus monolayers, respectively, schematically represented in Figure 1a. We studied their nonlinear optical response at room and cryogenic temperatures by focusing linearly polarized pulsed light of angular frequency ω onto the crystal, and detecting the outgoing light in reflection geometry, as illustrated in Figure 1a. In particular, we used 100-fs pulses with a repetition rate of 80 MHz generated by a tunable optical parametric oscillator (OPO) and pumped by a mode-locked Ti:sapphire laser (see Methods).

MoSSe and WSSe Janus monolayers are non-centrosymmetric crystals [15], and thus, possess nonvanishing even-order terms in the polarization vector expansion. As a result, they exhibit a distinct second harmonic (SH) overtone induced by a light field of frequency ω [57, 58]:

$$P_i^{(2)}(2\omega) = \epsilon_0 \sum_{j,k} \chi_{ijk}^{(2)}(2\omega; \omega, \omega) E_j(\omega) E_k(\omega) \quad (1)$$

here, Cartesian components of the second-order polarization vector $\mathbf{P}^{(2)}(2\omega)$ capture the material's response to the interaction with an external optical field $\mathbf{E}(\omega)$. The two vectors are linked *via* a third-rank tensor $\chi^{(2)}(2\omega, \omega, \omega)$, which can be directly deduced from the crystal symmetry. SHG is a parametric process where the annihilation of two photons of frequency ω is followed by the creation of a single photon of frequency 2ω . The photons link (virtual or real) excited states $|1\rangle$ and $|2\rangle$ to the electronic ground state $|0\rangle$ [58, 59], as illustrated in Figure 1b. In contrast, THG exists irrespective of the inversion symmetry and involves three annihilated photons of energy $\hbar\omega$ and a created photon of energy $3\hbar\omega$ from a state $|3\rangle$ denoted in purple in Figure 1b. Analogously to Eq. (1), third-order polarization properties of a crystal are dictated by a fourth-rank tensor $\chi^{(3)}(3\omega; \omega, \omega, \omega)$ [58].

In the case of TMDs, upon a two-photon excitation, the system may in addition relax *via* phonons Ω through a two-photon photoluminescence (TP-PL) involving a real exciton state $|R_{X^0}\rangle$ [60], denoted in light blue.

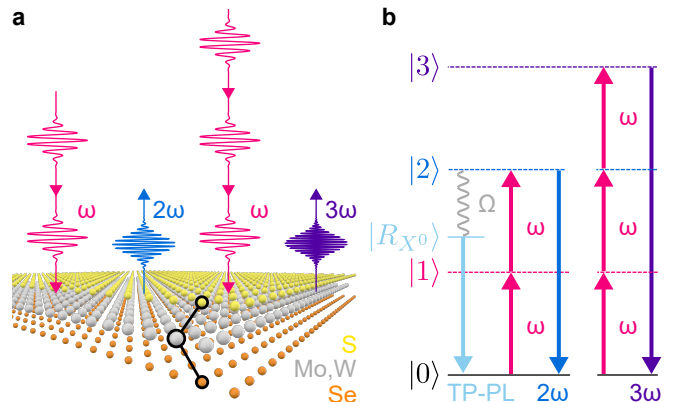


Figure 1. Harmonic generation in Janus TMD monolayers. (a) Schematic representation of a Janus TMD monolayer and the reflection measurement geometry. (b) Schematic representation of SHG (blue), THG (purple), and TP-PL (light blue) transitions under two- and three-photon excitation with angular frequency ω (magenta) between the excited levels $|1\rangle$, $|2\rangle$, $|3\rangle$, the real exciton level $|R_{X^0}\rangle$, linked *via* a phonon channel Ω to $|2\rangle$ (gray), and the ground state $|0\rangle$.

Figure 2a (2c) shows the detected light from MoSSe (WSSe) Janus monolayer at room temperature using $\hbar\omega = 0.92$ eV ($\hbar\omega = 1.03$ eV) excitation energy. For both materials, we detect a pronounced SHG signal (blue) and less efficient TP-PL signal (light blue) at a photon energy corresponding to the $1s$ neutral exciton X^0 at ~ 1.69 eV (~ 1.79 eV) [39]. Figures 2b and 2d show the power dependence of the SH signal for MoSSe and WSSe Janus monolayers, respectively, confirming the SH nature of the signal at $2\hbar\omega$ *via* the canonical quadratic increase in the SH peak power as a function of pump fluence [58, 61, 62]. In addition, we measure circular polarization selection rules consistent with SHG (see SI Section S1).

We also observe THG signals, with the pump laser close to the telecommunication C band. Figures 2e and 2g show room temperature SHG and THG spectra of MoSSe and WSSe Janus monolayers for excitation energies $\hbar\omega = 0.83$ eV and $\hbar\omega = 0.8$ eV, respectively. To confirm the third harmonic (TH) nature of the signal, we again perform power-dependent measurements which exhibit power law dependencies with near cubic behaviour, as expected [63–66]. The results are presented in Figure 2f for MoSSe, and Figure 2h for WSSe Janus monolayer, respectively. The intensity of the nonlinear response is normally expected to drop with increasing nonlinear order. However, for low pumping energies, TMDs exhibit a higher THG compared to the SHG signal due to nearly rotationally invariant bands only corrected by trigonal

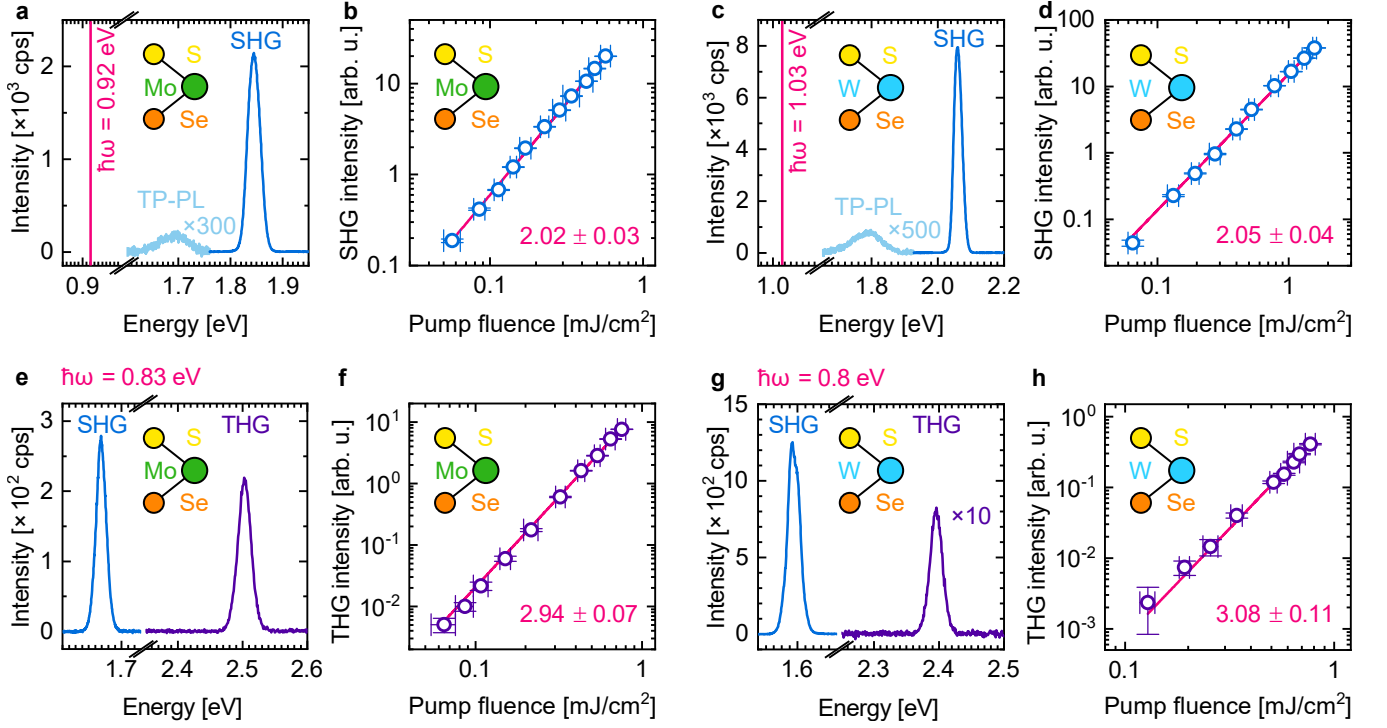


Figure 2. SHG and THG in MoSSe and WSSe Janus monolayers. (a,c) Measured spectra showing SHG (blue) and scaled TP-PL (light blue) peaks stemming from (a) MoSSe and (c) WSSe Janus monolayer upon two-photon excitation (magenta). (b,d) Respective SHG peak intensities as a function of pump fluence show quadratic increase as extracted from the power law fit (magenta). (e,g) THG (purple) and SHG (blue) spectra of (e) MoSSe Janus monolayer with excitation energy $\hbar\omega = 0.83$ eV and (g) WSSe Janus monolayer with excitation energy $\hbar\omega = 0.8$ eV. (f,h) Respective THG peak intensities as a function of pump fluence show cubic slopes as extracted from the power law fit (magenta).

warping of the valence and conduction bands [65, 67]. MoSSe Janus monolayers conform to this behavior, exhibiting comparable SHG and THG signals, as shown in Figure 2e. Here, THG does not dominate over SHG because the latter is close to resonance with the A exciton. Furthermore, we derive the value of the effective third-order susceptibility (see SI Section S2) and obtain $\chi_{\text{eff}}^{(3)}(\hbar\omega = 0.8 \text{ eV}) = 1.55 \times 10^5 \text{ pm}^2/\text{V}^2$ which is close to reported values for other TMDs [48, 63–66]. In terms of harmonic efficiency, defined as the ratio of THG peak power to incident power, we obtain $\sim 3 \times 10^{-11}$ for an incident power of 20 mW. Interestingly, in a WSSe Janus monolayer the SHG intensity dominates over the THG, in contrast to all measurements on TMDs reported to date. For WSSe Janus monolayer, the measured effective

third-order susceptibility is $\chi_{\text{eff}}^{(3)}(\hbar\omega = 0.83 \text{ eV}) = 1.52 \times 10^5 \text{ pm}^2/\text{V}^2$, and the harmonic efficiency is $\sim 10^{-11}$ for an incident power of 20 mW.

Next, we shift our attention to the study of the out-of-plane second-order nonlinear response of MoSSe Janus monolayer. In stark contrast to conventional TMDs, which belong to the D_{3h} point group, the lack of mirror symmetry puts Janus TMD monolayers in the C_{3v} point group, which displays five independent nonzero components $\chi_{xzx}^{(2)} = \chi_{yzy}^{(2)}$, $\chi_{xzx}^{(2)} = \chi_{yyz}^{(2)}$, $\chi_{zxx}^{(2)} = \chi_{zyy}^{(2)}$, $\chi_{zzz}^{(2)}$, $\chi_{yyy}^{(2)} = -\chi_{yxx}^{(2)} = -\chi_{xxy}^{(2)} = -\chi_{xyx}^{(2)}$. Furthermore, the Kleinman's symmetry condition in SHG always allows to permute the last two indices [58]; thus, $\chi_{xzx}^{(2)} = \chi_{xxz}^{(2)}$. Finally, we explicitly write the susceptibility tensor $\chi_{C_{3v}}^{(2)}(2\omega, \omega, \omega)$ in contracted notation [58] by rewriting Eq. (1) in a matrix form:

$$\begin{pmatrix} P_x^{(2)}(2\omega) \\ P_y^{(2)}(2\omega) \\ P_z^{(2)}(2\omega) \end{pmatrix} = \varepsilon_0 \begin{pmatrix} 0 & 0 & 0 & 0 & \chi_{xzx}^{(2)} & -\chi_{yyy}^{(2)} \\ -\chi_{yyy}^{(2)} & \chi_{yyy}^{(2)} & 0 & \chi_{xzx}^{(2)} & 0 & 0 \\ \chi_{zxx}^{(2)} & \chi_{zxx}^{(2)} & \chi_{zzz}^{(2)} & 0 & 0 & 0 \end{pmatrix} \begin{pmatrix} E_x(\omega)E_x(\omega) \\ E_y(\omega)E_y(\omega) \\ E_z(\omega)E_z(\omega) \\ 2E_y(\omega)E_z(\omega) \\ 2E_x(\omega)E_z(\omega) \\ 2E_x(\omega)E_y(\omega) \end{pmatrix} \quad (2)$$

Equation (2) implies two distinct features: (i) the presence of a nonvanishing out-of-plane $P_z^{(2)}(2\omega)$ polarization, as illustrated in the blue inset in Figure 3a, and (ii) the introduction of additional terms to the polarization vector components by an out-of-plane driving field $E_z(\omega)$, which can be activated by exciting the crystal at an angle, as illustrated in Figure 3a with a magenta line.

The experimentally accessible SHG intensity components can be conveniently derived from the polarization $P_{x,y,z}^{(2)}(2\omega)$ by introducing a polar coordinate system, as shown in Figure 3b. The resulting SHG intensity components are:

$$I_x \propto |\chi_{xxz}^{(2)} \sin 2\theta + \chi_{yyy}^{(2)} \cos^2 \theta \sin 3\phi|^2 \quad (3)$$

$$I_y \propto |\chi_{yyy}^{(2)} \cos^2 \theta \cos 3\phi|^2 \quad (4)$$

$$I_z \propto |\chi_{zxx}^{(2)} \cos^2 \theta + \chi_{zzz}^{(2)} \sin^2 \theta|^2 \quad (5)$$

where θ is the incidence angle of the excitation, ϕ is the crystal orientation angle, while excitation and detection light polarization are fixed along the x -axis [53]. In contrast, the SHG intensity components stemming from D_{3h} TMDs are [53, 62, 68]:

$$I_x \propto |\chi_{yyy}^{(2)} \cos^2 \theta \sin 3\phi|^2 \quad (6)$$

$$I_y \propto |\chi_{yyy}^{(2)} \cos^2 \theta \cos 3\phi|^2 \quad (7)$$

To extract the susceptibility tensor components of Janus TMD monolayers, we measure the SHG intensity as a function of the rotation angle ϕ of the excitation and detection polarizers in a co-polarized configuration (see Methods). This is equivalent to rotating the crystal in the reference frame with polarizers fixed along the x -axis. Therefore, we may use the aforementioned equations to model the experimentally collected SHG light intensity $I_p = I_x \cos^2 \theta + I_z \sin^2 \theta$, which sums both components present in the plane of incidence. We used a high-NA objective (NA = 0.75), which enables large angles θ for strong out-of-plane driving and high detection efficiency of the out-of-plane polarization component. This approach simplifies the methods previously employed to retrieve non-planar components [29, 69] and can easily be generalized for any material of a similar symmetry. Figure 3c plots normalized I_p as a function of ϕ on a logarithmic scale measured from a MoSSe Janus monolayer excited at $\hbar\omega = 0.885$ eV, away from the A exciton resonance to avoid the TP-PL signal. Following Eqs. (3) and (5), we expect that out-of-plane susceptibility components $\chi_{xxz}^{(2)}$, $\chi_{zxx}^{(2)}$, and $\chi_{zzz}^{(2)}$ contribute to the non-vanishing I_p for all angles ϕ . Indeed, the flower pattern 'opens up', never reaching zero, as shown in Figure 3c by

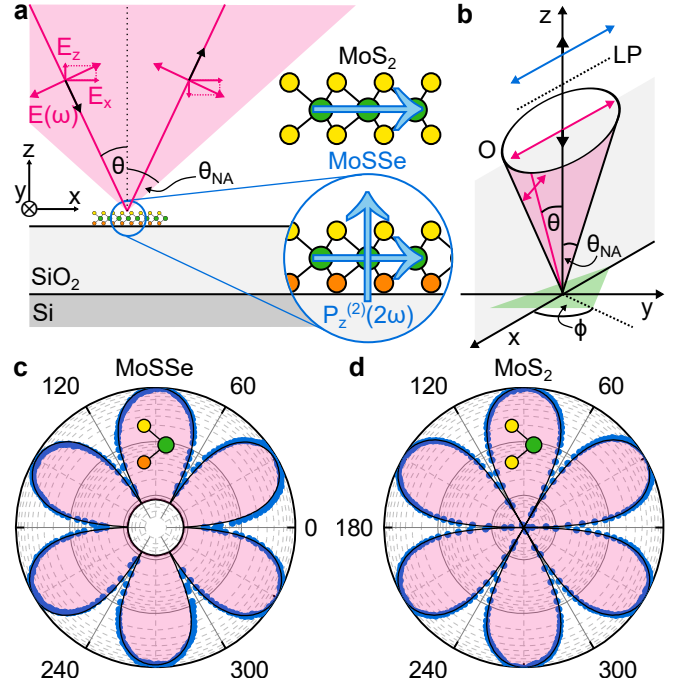


Figure 3. Out-of-plane polarization dipole in MoSSe Janus monolayer. (a) Schematic representation of the out-of-plane SH excitation and detection. Magenta denotes light incident along an angle θ from the optical axis, limited to θ_{NA} by the objective numerical aperture. MoSSe Janus monolayer possesses the $P_z^{(2)}(2\omega)$ component contrasting with the MoS_2 monolayer which only has an in-plane polarization component. (b) Schematic representation of the measurement configuration in a polar coordinate system. Excitation (magenta) and detection (blue) light have the same polarization entering and exiting the objective (O) determined with a linear polarizer (LP). Angle ϕ follows the crystal orientation. (c,d) Logarithmic polar plots of the normalized polarization-resolved SHG intensity of (c) Janus MoSSe and (d) MoS_2 monolayer. Measured intensity is represented with blue data points, the fitting curve in black, and the shaded region in pink is bound by the minimum of the fitting function.

the nonshaded region where the upper border represents the minimum value of the fitting function. Here, we take into account the angle-dependent substrate reflection and integrate the resulting intensity over the angle θ for the entire NA of the objective as explained in SI Section S3. In comparison, Figure 3d shows normalized polarization-resolved SHG intensity of a reference MoS_2 monolayer for the same excitation energy and the same-scaled logarithmic polar plot. I_p follows the characteristic six-fold pattern given by Eq. (6) which goes to zero when excitation polarization is aligned with the zigzag crystal edge [61, 62, 68], strongly contrasting with the MoSSe Janus monolayer in Figure 3c (see SI Section S4).

We now turn to disentangling the complex interplay of all susceptibility components contributing to the SHG intensity I_p . In order to give a quantitative estimate of the out-of-plane components compared to the in-plane

components, we simplify the $\chi^{(2)}$ tensor by imposing the Kleinman's symmetry to obtain $\chi_{xxz}^{(2)} = \chi_{zxx}^{(2)}$ [29, 58]. This is possible since under these specific experimental conditions the SHG process is performed far off exciton resonances. We further reduce the number of parameters by introducing a $\chi_{zzz}^{(2)}/\chi_{xxz}^{(2)}$ ratio deduced from theoretical calculations [53]. As a final result, we obtain $\chi_{yyy}^{(2)}/\chi_{xxz}^{(2)} = 8.4$ at $\hbar\omega = 0.885$ eV pumping (see SI Section S3), which is comparable to theoretically calculated values [53]. Thus, with our simple approach we are able to fully map the second-order susceptibility tensor in Janus TMD monolayers.

Finally, we discuss the second-order nonlinear dispersion at room and cryogenic temperatures in MoS₂ and WSe₂ Janus monolayers, focusing on the in-plane component $\chi_{yyy}^{(2)}$ of the nonlinear susceptibility. For this purpose, we use a low-NA objective (NA = 0.3) to quench the non-planar components with negligible out-of-plane driving. Figures 4a and 4b show MoS₂ Janus monolayer wavelength-dependent SHG spectra at room and cryogenic temperatures, respectively, obtained by sweeping the pumping energy, while maintaining constant pumping power. From the SHG intensities, we can derive the absolute values of the corresponding effective bulk-like second-order susceptibility dispersion $\chi_{yyy}^{(2)}$ [48, 64], presented in gray points and gray error band to account for excitation power fluctuations (see SI Section S2). For $\hbar\omega = 0.885$ eV excitation, we measure $\chi_{yyy}^{(2)} = 51$ pm/V. Then, we straightforwardly obtain the other components $\chi_{xxz}^{(2)} = \chi_{zxx}^{(2)} = 6$ pm/V, and $\chi_{zzz}^{(2)} = 1.5$ pm/V, where $\chi_{yyy}^{(2)}$ is highlighted in Figure 4a by the dotted line. Furthermore, when resonant to a real state, SHG is strongly enhanced [60] and it can thus be used as a spectroscopic tool to map the exciton states of Janus TMD monolayers. For the MoS₂ Janus monolayer, we observe pronounced resonances corresponding to the *A* and *B* excitons, and note that the *A* to *B* exciton $\chi_{yyy}^{(2)}$ ratio evolves from the *B* exciton dominating at room temperature to being the same as the *A* exciton at $T = 7$ K. This is in clear contrast to the WSe₂ Janus monolayer in Figures 4c and 4d at room and cryogenic temperatures, respectively. While *A* and *B* show similar values at $T = 10$ K, *A* dominates over *B* at room temperature. In addition, the WSe₂ Janus monolayer dispersion shows additional resonances below 1.8 eV the origin of which remains unclear at present and requires further study. We tentatively ascribe them to charged excitons or defect bands. At room temperature, the SH susceptibility of MoS₂ and WSe₂ Janus monolayers at exciton resonances is $\chi_{yyy}^{(2)} \approx 150$, and 200 pm/V, respectively, which is among the largest reported values of second-order susceptibilities for any TMD monolayer [70].

CONCLUSION

In summary, we studied optical nonlinearities in MoS₂ and WSe₂ Janus monolayers. We found an unusually low TH intensity in WSe₂. In addition, we introduced a simple method to study their out-of-plane nonlinear susceptibility and measured values of $\chi_{xxz}^{(2)} = \chi_{zxx}^{(2)} = 6$ pm/V and $\chi_{zzz}^{(2)} = 1.5$ pm/V in MoS₂ Janus monolayer. Finally, we provide the susceptibility dispersion on and off-resonance across the exciton spectrum of both materials at room and cryogenic temperatures. Close to exciton resonances, we measured up to $\chi_{yyy}^{(2)} \approx 200$ pm/V for the in-plane SH nonlinear susceptibility, a value that is among the largest measured for atomically thin materials. Our work establishes a solid foundation to understand the nonlinear optical response of Janus TMD monolayers and their use in applications such as broadband frequency conversion and nonlinear photonic integrated circuits.

METHODS

Samples. Janus TMD monolayers were synthesized *via* a room temperature selective epitaxy atomic replacement method thoroughly explained in ref. [33]. MoS₂ and WSe₂ Janus monolayers lay on Si/SiO₂ and Al₂O₃ substrates, respectively. The reference MoS₂ monolayer was encapsulated in thin hBN (HQ Graphene) and prepared on a Si/SiO₂ substrate with the same thickness as for MoS₂ Janus monolayer. SHG maps from prototypical MoS₂ and WSe₂ Janus monolayers are presented in SI Section S5.

Optical Measurements. 100-fs pulsed laser was used for SHG and THG measurements with a repetition rate of 80 MHz generated from an OPO (Levante IR fs, A.P.E.; and Inspire Femtosecond OPO, Radiantis) and pumped by a mode-locked Ti:sapphire laser, which was followed by a linear polarizer to ensure fixed excitation polarization.

For the polarization-resolved SHG measurements, a high-NA objective (NA = 0.75, Objective LD Plan-Neofluar 63x/0.75 Corr M27, Zeiss) was used to reveal out-of-plane susceptibility tensor components. A longpass dichroic mirror was used to separate the generated SHG from the fundamental and direct it onto a single channel detector (silicon avalanche photodiode, APD440A, Thorlabs). Co-polarized excitation-detection configuration and polarization rotation were achieved by positioning a linear polarizer and a half-waveplate between the objective and the dichroic mirror. Detection noise, substrate influence, and acceptance angle range were taken into account.

For wavelength-dependent SHG measurements in Figure 4, and SHG and THG measurements in Figure 2, a low-NA achromatic objective (NA = 0.3, 15x Reflec-

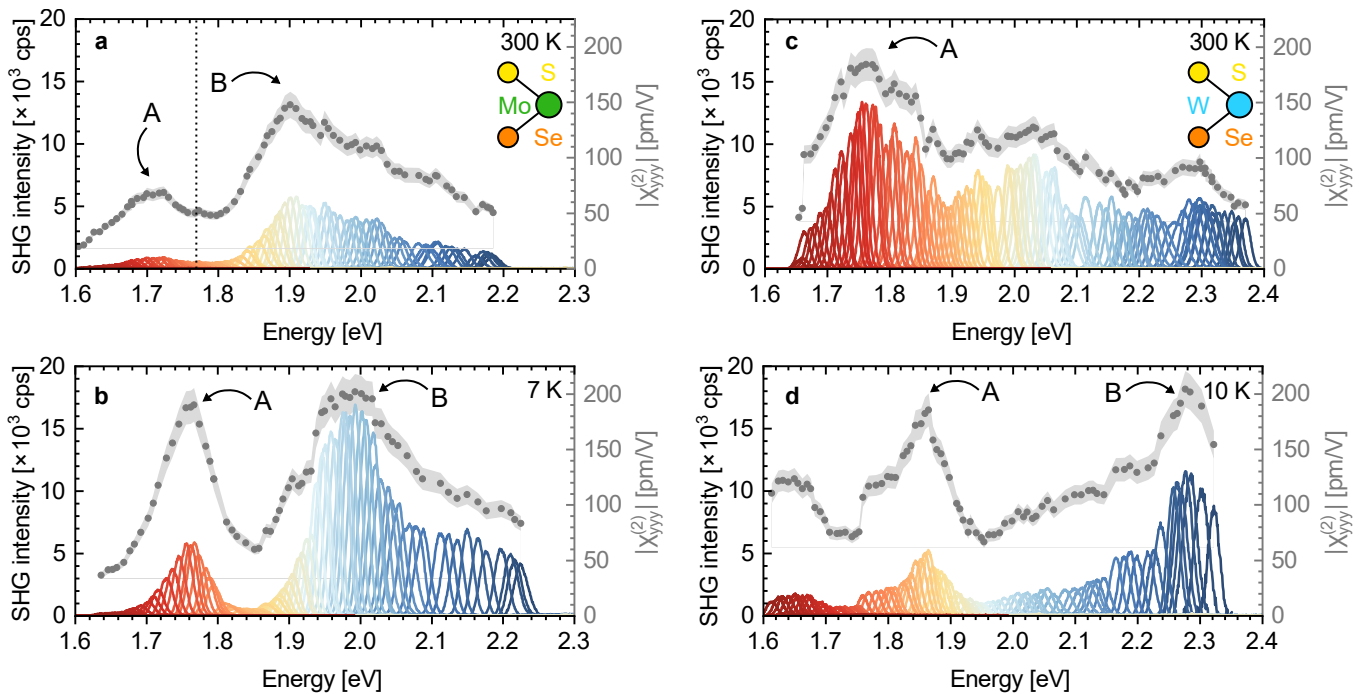


Figure 4. SHG enhancement at exciton resonances and $\chi_{yy}^{(2)}$ dispersion. (a,b) SHG spectra from MoSSe Janus monolayer as a function of two-photon energy at (a) $T = 300$ K and (b) $T = 7$ K with $\chi_{yy}^{(2)}$ dispersion represented in gray points within a light gray error band. (c,d) SHG spectra from WSSe Janus monolayer as a function of two-photon energy at (c) $T = 300$ K and (d) $T = 10$ K with $\chi_{yy}^{(2)}$ dispersion represented in gray points within a light gray error band. Assignments of A and B excitons are denoted by arrows.

tive microscope objective, Thorlabs) was used with a co-polarized excitation and detection polarizers. For cryogenic measurements a He-flow cryostat (Cryovac) was used. The collected light was analyzed in a spectrometer coupled to a charged-coupled device (Horiba).

SUPPORTING INFORMATION

Selection rules for circularly polarized light and conservation of the angular momentum. Effective bulk-like susceptibility. Polarization-resolved SHG intensity fitting function. Polarization-resolved SHG: MoSSe and MoS₂. SHG imaging of MoSSe and WSSe Janus monolayers.

AUTHOR CONTRIBUTIONS AND ACKNOWLEDGMENTS

M.M.P., G.S., J.J.F., and M.B. conceived and designed the experiment. Y.Q., Y.Sa., Y.Sh., and S.T. grew the Janus TMD monolayers, and A.B.M. fabricated the MoS₂ sample. M.M.P., V.V., P.H., and A.B.M. performed the optical measurements. M.M.P. analyzed the data and discussed them with all authors. M.M.P., G.S., and M.B. wrote the manuscript with input from all authors.

S.T. acknowledges primary support from DOE-SC0020653 (materials synthesis), NSF DMR 2111812 (for initial exciton characterization), NSF ECCS 2052527 (for electronic characterization), NSF DMR 2206987 (for magnetic purity tests), and NSF CMMI 2129412 for process optimization. K.M. and J.J.F. acknowledge support from the European Union Horizon 2020 research and innovation programme under Grant Agreement No. 820423 (S2QUIP) and the Deutsche Forschungsgemeinschaft (DFG, German Research Foundation) under Germany's Excellence Strategy – MCQST (EXC-2111), e-Conversion (EXC-2089), and via SPP 2299. M.M.P. acknowledges TUM International Graduate School of Science and Engineering (IGSSE). A.B.M. acknowledges funding from the International Max Planck Research School for Quantum Science and Technology (IMPRS-QST). M.B. and V.V. acknowledge the Alexander v. Humboldt foundation for financial support in the framework of their fellowship programs. K.M. acknowledges support from the Bayerische Akademie der Wissenschaften. G.S. acknowledges the German Research Foundation DFG (CRC 1375 NOA projects B5) and the IRTG 2675 META-ACTIVE (project A4). *The authors declare no competing financial interest.*

-
- * Marko.Petric@wsi.tum.de
† sefaattin.tongay@asu.edu
‡ giancarlo.soavi@uni-jena.de
§ Matteo.Barbone@wsi.tum.de
- [1] O. Dogadov, C. Trovatello, B. Yao, G. Soavi, and G. Cerullo, Parametric Nonlinear Optics with Layered Materials and Related Heterostructures, *Laser & Photonics Reviews* **16**, 2100726 (2022).
 - [2] S. Shree, D. Lagarde, L. Lombez, C. Robert, A. Balocchi, K. Watanabe, T. Taniguchi, X. Marie, I. C. Gerber, M. M. Glazov, L. E. Golub, B. Urbaszek, and I. Paradisanos, Interlayer exciton mediated second harmonic generation in bilayer MoS₂, *Nature Communications* **12**, 6894 (2021).
 - [3] I. Paradisanos, A. M. S. Raven, T. Amand, C. Robert, P. Renucci, K. Watanabe, T. Taniguchi, I. C. Gerber, X. Marie, and B. Urbaszek, Second harmonic generation control in twisted bilayers of transition metal dichalcogenides, *Physical Review B* **105**, 115420 (2022).
 - [4] K.-Q. Lin, S. Bange, and J. M. Lupton, Quantum interference in second-harmonic generation from monolayer WSe₂, *Nature Physics* **15**, 242 (2019).
 - [5] G. Soavi, G. Wang, H. Rostami, D. G. Purdie, D. De Fazio, T. Ma, B. Luo, J. Wang, A. K. Ott, D. Yoon, S. A. Bourelle, J. E. Muench, I. Goykhman, S. Dal Conte, M. Celebrano, A. Tomadin, M. Polini, G. Cerullo, and A. C. Ferrari, Broadband, electrically tunable third-harmonic generation in graphene, *Nature Nanotechnology* **13**, 583 (2018).
 - [6] S. Klimmer, O. Ghaebi, Z. Gan, A. George, A. Turchanin, G. Cerullo, and G. Soavi, All-optical polarization and amplitude modulation of second-harmonic generation in atomically thin semiconductors, *Nature Photonics* **15**, 837 (2021).
 - [7] Y. Zhang, Y. Wang, Y. Dai, X. Bai, X. Hu, L. Du, H. Hu, X. Yang, D. Li, Q. Dai, T. Hasan, and Z. Sun, Chirality logic gates, *Science Advances* **8**, eabq8246 (2022).
 - [8] Y. Li, N. An, Z. Lu, Y. Wang, B. Chang, T. Tan, X. Guo, X. Xu, J. He, H. Xia, Z. Wu, Y. Su, Y. Liu, Y. Rao, G. Soavi, and B. Yao, Nonlinear co-generation of graphene plasmons for optoelectronic logic operations, *Nature Communications* **13**, 3138 (2022).
 - [9] N. An, T. Tan, Z. Peng, C. Qin, Z. Yuan, L. Bi, C. Liao, Y. Wang, Y. Rao, G. Soavi, and B. Yao, Electrically Tunable Four-Wave-Mixing in Graphene Heterogeneous Fiber for Individual Gas Molecule Detection, *Nano Letters* **20**, 6473 (2020).
 - [10] A. Dasgupta, J. Gao, and X. Yang, Atomically Thin Nonlinear Transition Metal Dichalcogenide Holograms, *Nano Letters* **19**, 6511 (2019).
 - [11] Q. Guo, X.-Z. Qi, L. Zhang, M. Gao, S. Hu, W. Zhou, W. Zhang, X. Zhao, J. Wang, B. Yan, M. Xu, Y.-K. Wu, G. Eda, Z. Xiao, S. A. Yang, H. Gou, Y. P. Feng, G.-C. Guo, W. Zhou, X.-F. Ren, C.-W. Qiu, S. J. Pennycook, and A. T. S. Wee, Ultrathin quantum light source with van der Waals NbOCl₂ crystal, *Nature* **613**, 53 (2023).
 - [12] F. Li, W. Wei, P. Zhao, B. Huang, and Y. Dai, Electronic and Optical Properties of Pristine and Vertical and Lateral Heterostructures of Janus MoSSe and WSSe, *The Journal of Physical Chemistry Letters* **8**, 5959 (2017).
 - [13] J. Wang, H. Shu, T. Zhao, P. Liang, N. Wang, D. Cao, and X. Chen, Intriguing electronic and optical properties of two-dimensional Janus transition metal dichalcogenides, *Physical Chemistry Chemical Physics* **20**, 18571 (2018).
 - [14] W. Shi and Z. Wang, Mechanical and electronic properties of Janus monolayer transition metal dichalcogenides, *Journal of Physics: Condensed Matter* **30**, 215301 (2018).
 - [15] Y. C. Cheng, Z. Y. Zhu, M. Tahir, and U. Schwingenschlögl, Spin-orbit-induced spin splittings in polar transition metal dichalcogenide monolayers, *EPL (Europhysics Letters)* **102**, 57001 (2013).
 - [16] C. Cheng, J.-T. Sun, X.-R. Chen, H.-X. Fu, and S. Meng, Nonlinear Rashba spin splitting in transition metal dichalcogenide monolayers, *Nanoscale* **8**, 17854 (2016).
 - [17] Q.-F. Yao, J. Cai, W.-Y. Tong, S.-J. Gong, J.-Q. Wang, X. Wan, C.-G. Duan, and J. H. Chu, Manipulation of the large Rashba spin splitting in polar two-dimensional transition-metal dichalcogenides, *Physical Review B* **95**, 165401 (2017).
 - [18] T. Hu, F. Jia, G. Zhao, J. Wu, A. Stroppa, and W. Ren, Intrinsic and anisotropic Rashba spin splitting in Janus transition-metal dichalcogenide monolayers, *Physical Review B* **97**, 235404 (2018).
 - [19] M. Adhib Ulil Absor, H. Kotaka, F. Ishii, and M. Saito, Tunable spin splitting and spin lifetime in polar WSTe monolayer, *Japanese Journal of Applied Physics* **57**, 04FP01 (2018).
 - [20] S. Patel, U. Dey, N. P. Adhikari, and A. Taraphder, Electric field and strain-induced band-gap engineering and manipulation of the Rashba spin splitting in Janus van der Waals heterostructures, *Physical Review B* **106**, 035125 (2022).
 - [21] J. Yuan, Y. Yang, Y. Cai, Y. Wu, Y. Chen, X. Yan, and L. Shen, Intrinsic skyrmions in monolayer Janus magnets, *Physical Review B* **101**, 094420 (2020).
 - [22] J. Liang, W. Wang, H. Du, A. Hallal, K. Garcia, M. Chshiev, A. Fert, and H. Yang, Very large Dzyaloshinskii-Moriya interaction in two-dimensional Janus manganese dichalcogenides and its application to realize skyrmion states, *Physical Review B* **101**, 184401 (2020).
 - [23] Q. Cui, J. Liang, Z. Shao, P. Cui, and H. Yang, Strain-tunable ferromagnetism and chiral spin textures in two-dimensional Janus chromium dichalcogenides, *Physical Review B* **102**, 094425 (2020).
 - [24] H. Jin, T. Wang, Z.-R. Gong, C. Long, and Y. Dai, Prediction of an extremely long exciton lifetime in a Janus-MoSTe monolayer, *Nanoscale* **10**, 19310 (2018).
 - [25] F. Li, W. Wei, H. Wang, B. Huang, Y. Dai, and T. Jacob, Intrinsic Electric Field-Induced Properties in Janus MoSSe van der Waals Structures, *The Journal of Physical Chemistry Letters* **10**, 559 (2019).
 - [26] C. Long, Y. Dai, Z.-R. Gong, and H. Jin, Robust type-II band alignment in Janus-MoSSe bilayer with extremely long carrier lifetime induced by the intrinsic electric field, *Physical Review B* **99**, 115316 (2019).
 - [27] T. Zheng, Y.-C. Lin, Y. Yu, P. Valencia-Acuna, A. A. Puretzky, R. Torsi, C. Liu, I. N. Ivanov, G. Duscher, D. B. Geohegan, Z. Ni, K. Xiao, and H. Zhao, Excitonic Dynamics in Janus MoSSe and WSSe Monolayers, *Nano Letters* **21**, 931 (2021).
 - [28] H. Guo, X. Zhang, and G. Lu, Tuning moiré excitons in Janus heterobilayers for high-temperature Bose-Einstein

- condensation, *Science Advances* **8**, eabp9757 (2022).
- [29] A.-Y. Lu, H. Zhu, J. Xiao, C.-P. Chuu, Y. Han, M.-H. Chiu, C.-C. Cheng, C.-W. Yang, K.-H. Wei, Y. Yang, Y. Wang, D. Sokaras, D. Nordlund, P. Yang, D. A. Muller, M.-Y. Chou, X. Zhang, and L.-J. Li, Janus monolayers of transition metal dichalcogenides, *Nature Nanotechnology* **12**, 744 (2017).
- [30] J. Zhang, S. Jia, I. Kholmanov, L. Dong, D. Er, W. Chen, H. Guo, Z. Jin, V. B. Shenoy, L. Shi, and J. Lou, Janus Monolayer Transition-Metal Dichalcogenides, *ACS Nano* **11**, 8192 (2017).
- [31] D. Lam, D. Lebedev, and M. C. Hersam, Morphotaxy of Layered van der Waals Materials, *ACS Nano* **16**, 7144 (2022).
- [32] Y.-C. Lin, C. Liu, Y. Yu, E. Zarkadoula, M. Yoon, A. A. Puzos, L. Liang, X. Kong, Y. Gu, A. Strasser, H. M. Meyer, M. Lorenz, M. F. Chisholm, I. N. Ivanov, C. M. Rouleau, G. Duscher, K. Xiao, and D. B. Geohegan, Low Energy Implantation into Transition-Metal Dichalcogenide Monolayers to Form Janus Structures, *ACS Nano* **14**, 3896 (2020).
- [33] D. B. Trivedi, G. Turgut, Y. Qin, M. Y. Sayyad, D. Hajra, M. Howell, L. Liu, S. Yang, N. H. Pattoary, H. Li, M. M. Petrić, M. Meyer, M. Kremser, M. Barbone, G. Soavi, A. V. Stier, K. Müller, S. Yang, I. S. Esqueda, H. Zhuang, J. J. Finley, and S. Tongay, Room-Temperature Synthesis of 2D Janus Crystals and their Heterostructures, *Advanced Materials* **32**, 2006320 (2020).
- [34] Y. Guo, Y. Lin, K. Xie, B. Yuan, J. Zhu, P.-C. Shen, A.-Y. Lu, C. Su, E. Shi, K. Zhang, C. HuangFu, H. Xu, Z. Cai, J.-H. Park, Q. Ji, J. Wang, X. Dai, X. Tian, S. Huang, L. Dou, L. Jiao, J. Li, Y. Yu, J.-C. Idrobo, T. Cao, T. Palacios, and J. Kong, Designing artificial two-dimensional landscapes via atomic-layer substitution, *Proceedings of the National Academy of Sciences* **118**, e2106124118 (2021).
- [35] C. W. Jang, W. J. Lee, J. K. Kim, S. M. Park, S. Kim, and S.-H. Choi, Growth of two-dimensional Janus MoSSe by a single in situ process without initial or follow-up treatments, *NPG Asia Materials* **14**, 15 (2022).
- [36] Y. Qin, M. Sayyad, A. R.-P. Montblanch, M. S. G. Feuer, D. Dey, M. Blei, R. Sailus, D. M. Kara, Y. Shen, S. Yang, A. S. Botana, M. Atature, and S. Tongay, Reaching the Excitonic Limit in 2D Janus Monolayers by In Situ Deterministic Growth, *Advanced Materials* **34**, 2106222 (2022).
- [37] Z. Gan, I. Paradisanos, A. Estrada-Real, J. Picker, E. Najafidehaghani, F. Davies, C. Neumann, C. Robert, P. Wiecha, K. Watanabe, T. Taniguchi, X. Marie, J. Biskupek, M. Mundsinger, R. Leiter, U. Kaiser, A. V. Krasheninnikov, B. Urbaszek, A. George, and A. Turchanin, Chemical Vapor Deposition of High-Optical-Quality Large-Area Monolayer Janus Transition Metal Dichalcogenides, *Advanced Materials* **34**, 2205226 (2022).
- [38] S. B. Harris, Y.-C. Lin, A. A. Puzos, L. Liang, O. Dyck, T. Berlijn, G. Eres, C. M. Rouleau, K. Xiao, and D. B. Geohegan, Real-Time Diagnostics of 2D Crystal Transformations by Pulsed Laser Deposition: Controlled Synthesis of Janus WSSe Monolayers and Alloys, *ACS Nano*, acsnano.2c09952 (2023).
- [39] M. M. Petrić, M. Kremser, M. Barbone, Y. Qin, Y. Sayyad, Y. Shen, S. Tongay, J. J. Finley, A. R. Botello-Méndez, and K. Müller, Raman spectrum of Janus transition metal dichalcogenide monolayers WSSe and MoSSe, *Physical Review B* **103**, 035414 (2021).
- [40] K. Zhang, Y. Guo, D. T. Larson, Z. Zhu, S. Fang, E. Kaxiras, J. Kong, and S. Huang, Spectroscopic Signatures of Interlayer Coupling in Janus MoSSe/MoS₂ Heterostructures, *ACS Nano* **15**, 14394 (2021).
- [41] K. Zhang, Y. Guo, Q. Ji, A.-Y. Lu, C. Su, H. Wang, A. A. Puzos, D. B. Geohegan, X. Qian, S. Fang, E. Kaxiras, J. Kong, and S. Huang, Enhancement of van der Waals Interlayer Coupling through Polar Janus MoSSe, *Journal of the American Chemical Society* **142**, 17499 (2020).
- [42] T. Zheng, Y.-C. Lin, N. Rafizadeh, D. B. Geohegan, Z. Ni, K. Xiao, and H. Zhao, Janus Monolayers for Ultrafast and Directional Charge Transfer in Transition Metal Dichalcogenide Heterostructures, *ACS Nano* **16**, 4197 (2022).
- [43] J. Zhang, X. Wen, T. Zhai, G. P. Wiederrecht, and J. Lou, Unconventional optical properties of 2D Janus SMOSe induced by structural asymmetry, *2D Materials* **9**, 035006 (2022).
- [44] N. Youngblood and M. Li, Integration of 2D materials on a silicon photonics platform for optoelectronics applications, *Nanophotonics* **6**, 1205 (2016).
- [45] P. Tonndorf, O. Del Pozo-Zamudio, N. Gruhler, J. Kern, R. Schmidt, A. I. Dmitriev, A. P. Bakhtinov, A. I. Tartakovskii, W. Pernice, S. Michaelis de Vasconcellos, and R. Bratschitsch, On-Chip Waveguide Coupling of a Layered Semiconductor Single-Photon Source, *Nano Letters* **17**, 5446 (2017).
- [46] Y. Guo, Z. Li, N. An, Y. Guo, Y. Wang, Y. Yuan, H. Zhang, T. Tan, C. Wu, B. Peng, G. Soavi, Y. Rao, and B. Yao, A Monolithic Graphene-Functionalized Micro-laser for Multispecies Gas Detection, *Advanced Materials* **34**, 2207777 (2022).
- [47] G. Q. Ngo, E. Najafidehaghani, Z. Gan, S. Khazaei, M. P. Siems, A. George, E. P. Schartner, S. Nolte, H. Ebendorff-Heidepriem, T. Pertsch, A. Tuniz, M. A. Schmidt, U. Peschel, A. Turchanin, and F. Eilenberger, In-fibre second-harmonic generation with embedded two-dimensional materials, *Nature Photonics* **16**, 769 (2022).
- [48] A. Autere, H. Jussila, A. Marini, J. R. M. Saavedra, Y. Dai, A. Säynätjoki, L. Karvonen, H. Yang, B. Amirsolaimani, R. A. Norwood, N. Peyghambarian, H. Lipsanen, K. Kieu, F. J. G. de Abajo, and Z. Sun, Optical harmonic generation in monolayer group-VI transition metal dichalcogenides, *Physical Review B* **98**, 115426 (2018).
- [49] M. Zhao, Z. Ye, R. Suzuki, Y. Ye, H. Zhu, J. Xiao, Y. Wang, Y. Iwasa, and X. Zhang, Atomically phase-matched second-harmonic generation in a 2D crystal, *Light: Science & Applications* **5**, e16131 (2016).
- [50] C. Trovatiello, A. Marini, X. Xu, C. Lee, F. Liu, N. Currelli, C. Manzoni, S. Dal Conte, K. Yao, A. Ciattoni, J. Hone, X. Zhu, P. J. Schuck, and G. Cerullo, Optical parametric amplification by monolayer transition metal dichalcogenides, *Nature Photonics* **15**, 6 (2021).
- [51] Y. Wei, X. Xu, S. Wang, W. Li, and Y. Jiang, Second harmonic generation in Janus MoSSe a monolayer and stacked bulk with vertical asymmetry, *Physical Chemistry Chemical Physics* **21**, 21022 (2019).
- [52] A. Strasser, H. Wang, and X. Qian, Nonlinear Optical and Photocurrent Responses in Janus MoSSe Monolayer and MoS₂-MoSSe van der Waals Heterostructure, *Nano Letters* **22**, 4145 (2022).

- [53] N. A. Pike and R. Pachter, Angular Dependence of the Second-Order Nonlinear Optical Response in Janus Transition Metal Dichalcogenide Monolayers, *The Journal of Physical Chemistry C* **126**, 16243 (2022).
- [54] M.-E. Kleemann, R. Chikkaraddy, E. M. Alexeev, D. Kos, C. Carnegie, W. Deacon, A. C. de Pury, C. Große, B. de Nijs, J. Mertens, A. I. Tartakovskii, and J. J. Baumberg, Strong-coupling of WSe₂ in ultra-compact plasmonic nanocavities at room temperature, *Nature Communications* **8**, 1296 (2017).
- [55] M. Stührenberg, B. Munkhbat, D. G. Baranov, J. Cuadra, A. B. Yankovich, T. J. Antosiewicz, E. Olsson, and T. Shegai, Strong Light-Matter Coupling between Plasmons in Individual Gold Bi-pyramids and Excitons in Mono- and Multilayer WSe₂, *Nano Letters* **18**, 5938 (2018).
- [56] J. Zhang, W. Zhao, P. Yu, G. Yang, and Z. Liu, Second harmonic generation in 2D layered materials, *2D Materials* **7**, 042002 (2020).
- [57] Y. R. Shen, *The Principles of Nonlinear Optics*, wiley classics library ed ed., Wiley Classics Library (Wiley-Interscience, Hoboken, N.J., 2003).
- [58] R. W. Boyd, *Nonlinear Optics*, 3rd ed. (Academic Press, Amsterdam ; Boston, 2008).
- [59] P. A. Franken, A. E. Hill, C. W. Peters, and G. Weinreich, Generation of Optical Harmonics, *Physical Review Letters* **7**, 118 (1961).
- [60] G. Wang, X. Marie, I. Gerber, T. Amand, D. Lagarde, L. Bouet, M. Vidal, A. Balocchi, and B. Urbaszek, Giant Enhancement of the Optical Second-Harmonic Emission of WSe₂ Monolayers by Laser Excitation at Exciton Resonances, *Physical Review Letters* **114**, 097403 (2015).
- [61] L. M. Malard, T. V. Alencar, A. P. M. Barboza, K. F. Mak, and A. M. de Paula, Observation of intense second harmonic generation from MoS₂ atomic crystals, *Physical Review B* **87**, 201401 (2013).
- [62] N. Kumar, S. Najmaei, Q. Cui, F. Ceballos, P. M. Ajayan, J. Lou, and H. Zhao, Second harmonic microscopy of monolayer MoS₂, *Physical Review B* **87**, 161403 (2013).
- [63] R. Wang, H.-C. Chien, J. Kumar, N. Kumar, H.-Y. Chiu, and H. Zhao, Third-Harmonic Generation in Ultrathin Films of MoS₂, *ACS Applied Materials & Interfaces* **6**, 314 (2014).
- [64] R. I. Woodward, R. T. Murray, C. F. Phelan, R. E. P. de Oliveira, T. H. Runcorn, E. J. R. Kelleher, S. Li, E. C. de Oliveira, G. J. M. Fecine, G. Eda, and C. J. S. de Matos, Characterization of the second- and third-order nonlinear optical susceptibilities of monolayer MoS₂ using multiphoton microscopy, *2D Materials* **4**, 011006 (2016).
- [65] A. Säynätjoki, L. Karvonen, H. Rostami, A. Autere, S. Mehravar, A. Lombardo, R. A. Norwood, T. Hasan, N. Peyghambarian, H. Lipsanen, K. Kieu, A. C. Ferrari, M. Polini, and Z. Sun, Ultra-strong nonlinear optical processes and trigonal warping in MoS₂ layers, *Nature Communications* **8**, 893 (2017).
- [66] H. G. Rosa, Y. W. Ho, I. Verzhbitskiy, M. J. F. L. Rodrigues, T. Taniguchi, K. Watanabe, G. Eda, V. M. Pereira, and J. C. V. Gomes, Characterization of the second- and third-harmonic optical susceptibilities of atomically thin tungsten diselenide, *Scientific Reports* **8**, 10035 (2018).
- [67] A. Kormányos, V. Zólyomi, N. D. Drummond, P. Rakyta, G. Burkard, and V. I. Fal'ko, Monolayer MoS₂: Trigonal warping, the Γ valley, and spin-orbit coupling effects, *Physical Review B* **88**, 045416 (2013).
- [68] Y. Li, Y. Rao, K. F. Mak, Y. You, S. Wang, C. R. Dean, and T. F. Heinz, Probing Symmetry Properties of Few-Layer MoS₂ and h-BN by Optical Second-Harmonic Generation, *Nano Letters* **13**, 3329 (2013).
- [69] J. Xiao, H. Zhu, Y. Wang, W. Feng, Y. Hu, A. Dasgupta, Y. Han, Y. Wang, D. A. Muller, L. W. Martin, P. Hu, and X. Zhang, Intrinsic Two-Dimensional Ferroelectricity with Dipole Locking, *Physical Review Letters* **120**, 227601 (2018).
- [70] L. Lafeta, A. Corradi, T. Zhang, E. Kahn, I. Bilgin, B. R. Carvalho, S. Kar, M. Terrones, and L. M. Malard, Second- and third-order optical susceptibilities across exciton states in 2D monolayer transition metal dichalcogenides, *2D Materials* **8**, 035010 (2021).

SUPPORTING INFORMATION: Nonlinear Dispersion Relation and Out-of-Plane Second Harmonic Generation in MoSSe and WSSe Janus Monolayers

Marko M. Petrić,^{1,2,*} Viviana Villafañe,^{3,2} Paul Herrmann,⁴ Amine Ben Mhenni,^{3,2} Ying Qin,⁵ Yasir Sayyad,⁵ Yuxia Shen,⁵ Sefaattin Tongay,^{5,†} Kai Müller,^{1,2} Giancarlo Soavi,^{4,6,‡} Jonathan J. Finley,^{3,2} and Matteo Barbone^{1,2,§}

¹Walter Schottky Institut and Department of Electrical and Computer Engineering,
Technische Universität München, Am Coulombwall 4, 85748 Garching, Germany

²Munich Center for Quantum Science and Technology (MCQST), Schellingstrasse 4, 80799 Munich, Germany

³Walter Schottky Institut and Physik-Department,
Technische Universität München, Am Coulombwall 4, 85748 Garching, Germany

⁴Institute of Solid State Physics, Friedrich Schiller University Jena, Max-Wien-Platz 1, Jena, 07743 Germany

⁵Materials Science and Engineering, School for Engineering of Matter,
Transport and Energy, Arizona State University, Tempe, Arizona 85287, USA

⁶Abbe Center of Photonics, Friedrich Schiller University Jena, Albert-Einstein-Straße 6, 07745 Jena, Germany

SELECTION RULES FOR CIRCULARLY POLARIZED LIGHT AND CONSERVATION OF THE ANGULAR MOMENTUM

When exciting a crystal with a circularly polarized fundamental beam at normal incidence, conservation of out-of-plane angular momentum allows for transitions that obey:

$$\Delta L_{\text{photon}} = \Delta L_{\text{valley}} + \Delta L_{\text{exciton}} + \Delta L_{\text{lattice}}. \quad (\text{S1})$$

Here, $\Delta L_{\text{photon}} = \Delta m\hbar$, $\Delta L_{\text{valley}} = \Delta\tau\hbar$, $\Delta L_{\text{exciton}} = \Delta l\hbar$, and $\Delta L_{\text{lattice}} = \pm 3n\hbar$ (for crystals with a three-fold rotational symmetry) stand for changes in angular momenta of photons, valley, excitons, and crystal lattice, respectively [1, 2]. In the case of the 1s-exciton resonant SHG, exciton angular momentum does not flip, while the valley angular momentum has zero net change upon transition of the system from the ground state to the excited state and back; thus, Eq. (S1) can be simplified to $\Delta m\hbar = \pm 3\hbar$ ($n = 1$). The left side represents the net change of the spin of the photons, while the right side represents the angular momentum transferred to the crystal, which comes in integer number n of $\pm 3\hbar$ as a direct result of the three-fold crystal symmetry [1, 2]. Therefore, SHG emission always results in the opposite helicity of the incident light since $L_{\text{out}\sigma\pm} - 2L_{\text{in}\sigma\mp} = \pm 3\hbar$, where L_{in} and L_{out} stand for angular momenta of incoming and outgoing photons, and $L_{\sigma\pm} = \pm\hbar$.

This behavior holds for MoSSe and WSSe monolayers at room temperature as presented in Figures S1a and S1b, respectively. Here, left (right) panels show that pumping a left (right) circularly polarized light results in a strong right (left) circularly polarized SH signal and a highly suppressed left (right) circularly polarized SH signal. We tuned the two-photon energy above the real exciton transition for MoSSe and resonant to it for WSSe Janus monolayer. Measured SHG intensities $I_{\sigma\pm}$ result in a high degree of circular polarization $|(I_{\sigma\pm} - I_{\sigma\mp})/(I_{\sigma\pm} + I_{\sigma\mp})| = 96 - 99\%$, which is due to a parametric nature of the SHG, which is robust to the valley scattering [2–4]. Furthermore, this behavior should hold irrespective of the excitation energy, as the selection rule $\Delta m\hbar = \pm 3\hbar$ is ultimately independent of the valley degree of freedom and stems solely from the three-fold crystal symmetry, a property retained in all TMD monolayers.

EFFECTIVE BULK-LIKE SUSCEPTIBILITY

As demonstrated in Figures 2b and 2d (2f and 2h) in the main text, SHG (THG) intensity $P_{\text{SHG}}(2\omega)$ ($P_{\text{THG}}(3\omega)$) has quadratic (cubic) dependence with respect to the pump power $P_1(\omega)$ [5]:

$$P_{\text{SHG}}(2\omega) = \frac{16\sqrt{2}S|\chi^{(2)}|^2\omega^2}{c^3\epsilon_0^2 f\pi r^2 t_{\text{fwhm}}(1+n_2)^6} P_1^2(\omega) \quad (\text{S2})$$

$$P_{\text{SHG}}(3\omega) = \frac{64\sqrt{3}S^2|\chi^{(3)}|^2\omega^2}{c^4\epsilon_0^2 (ft_{\text{fwhm}}\pi r^2)^2(1+n_2)^8} P_1^3(\omega) \quad (\text{S3})$$

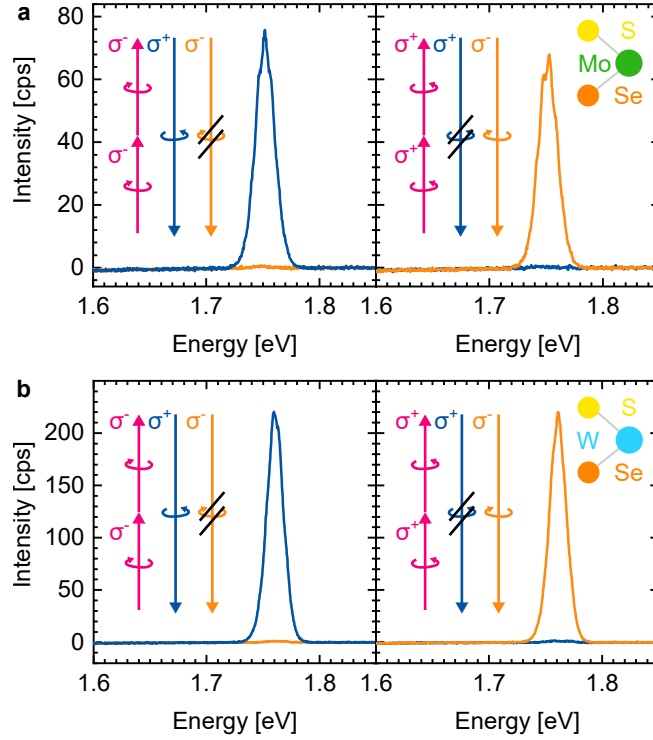


Figure S1. SHG polarization selection rules. (a,b) SHG spectra with σ^+ (dark blue) and σ^- (orange) circular-polarization filtering in the detection upon σ^- (left panel) and σ^+ (right panel) two-photon excitation (magenta arrows) for (a) MoSSe and (b) WSSe Janus monolayers.

Here, ω is the pumping angular frequency, $S = 0.94$ is a Gaussian pulse shape factor, $f = 80$ MHz is the pump laser repetition rate, $t_{\text{fwhm}} = 100$ fs is the pulse length, n_2 is the substrate refractive index, c is the speed of light in vacuum, ϵ_0 is the permittivity of free-space, and πr^2 is the laser spot area. Second-order susceptibility $\chi^{(2)}$ and third-order susceptibility $\chi^{(3)}$ can be thus derived from Eqs. S2 and S3, where SHG and THG power can be extracted from the area of measured spectral peaks. Finally, in the main text, we provide values of effective bulk-like susceptibilities (Figure 4 in the main text for $\chi_{yyy}^{(2)}$ and Figures 2f and 2h for $\chi_{\text{eff}}^{(3)}$) common in the literature, which are related to the susceptibilities in Eqs. S2 and S3 as [5, 6]:

$$|\chi_{\text{eff}}^{(2,3)}| = |\chi^{(2,3)}|/h \quad (\text{S4})$$

where h is a monolayer thickness ($h_{\text{MoSSe}} = 0.65$ nm). To finally obtain $\chi^{(2)}$ values presented in the main text, we also take into account the efficiency of the setup.

POLARIZATION-RESOLVED SHG INTENSITY FITTING FUNCTION

To arrive at different SHG intensities $I_{x,y,z}$ for the specific measurement configuration, we start from Eq. (2) in the main text and transform the incident electric field to polar coordinates. The resulting expressions are equivalent to the set of equations (9) in ref. [7] for polarization angle $\alpha = 0$, corresponding to the co-polarized configuration we use in our measurements:

$$I_x \propto |\chi_{xxz}^{(2)} \sin 2\theta + \chi_{yyy}^{(2)} \cos^2 \theta \sin 3\phi|^2 \quad (\text{S5})$$

$$I_y \propto |\chi_{yyy}^{(2)} \cos^2 \theta \cos 3\phi|^2 \quad (\text{S6})$$

$$I_z \propto |\chi_{zxx}^{(2)} \cos^2 \theta + \chi_{zzz}^{(2)} \sin^2 \theta|^2 \quad (\text{S7})$$

which are equivalent to Eqs. (3)–(5) in the main text. However, these intensities do not take substrate effects into account. Furthermore, they only predict values for a specific excitation angle θ and not the full range within the objective acceptance angle. In the following lines, we incorporate these two points to Eqs. S5, S6, and S7 to obtain the measured intensity I_p probed in our experiment.

The electric field impinging on the MoSSe Janus monolayer interferes with the reflected light from the substrate; thus, causing the following input electric field components, sketched in Figure S2 [8]:

$$E_x \rightarrow E_x(1 - r) \quad (\text{S8})$$

$$E_z \rightarrow E_z(1 + r) \quad (\text{S9})$$

$$r = \frac{r_{12} + \exp(i2\delta)r_{23}}{1 + \exp(i2\delta)r_{12}r_{23}} \quad (\text{S10})$$

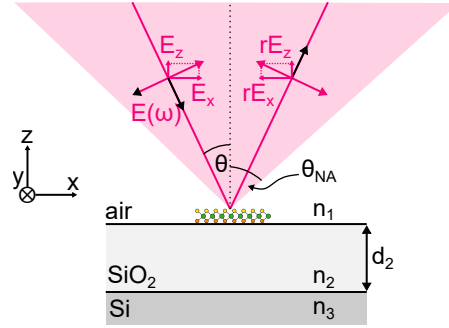


Figure S2. Incoming light field $E(\omega)$ from the objective focused onto MoSSe Janus monolayer. Magenta denotes light coming by an angle θ from the optical axis (dotted line), limited to θ_{NA} by the objective numerical aperture. Refractive indices $n_{1,2,3}$ stand for air, SiO_2 (of thickness $d_2 = 285$ nm) and Si (quasi-infinite thickness), respectively. Total reflection coefficient r can be calculated from Eq. S9.

Here, r is the total reflection coefficient for three different media in Figure S2, where we neglect the effect from the monolayer due to its small thickness; r_{ij} are reflection coefficients between interfaces i and j ($i, j = 1, 2, 3$), δ is the accumulated phase in the medium 2 (SiO_2) of thickness $d_2 = 285$ nm for the light of wavelength $\lambda = 1400$ nm. Coefficients r_{ij} and phase δ can be explicitly written as:

$$\delta = \frac{2\pi d_2}{\lambda} n_2 \cos \theta_2 \quad (\text{S11})$$

$$r_{ij} = \frac{n_j \cos \theta_i - n_i \cos \theta_j}{n_j \cos \theta_i + n_i \cos \theta_j} \quad (\text{S12})$$

Eq. S12 is one of the well-known Fresnel equations, where $n_{i,j}$ and $\theta_{i,j}$ are refractive indices and light incidence angles with respect to the z -axis, respectively. Different refraction angles are connected *via* Snell-Descartes law:

$$n_i \cos \theta_i = n_j \cos \theta_j \quad (\text{S13})$$

By performing matrix multiplication in Eq. (2) in the main text and incorporating new values for the input fields in Eqs. S9 and S10, we arrive at more accurate expressions for $I_{x,y,z}$:

$$I_x \propto |\chi_{xxz}^{(2)}(1 - r)(1 + r) \sin 2\theta + \chi_{yyy}^{(2)}(1 - r)^2 \cos^2 \theta \sin 3\phi|^2 \quad (\text{S14})$$

$$I_y \propto |\chi_{yyy}^{(2)}(1 - r)^2 \cos^2 \theta \cos 3\phi|^2 \quad (\text{S15})$$

$$I_z \propto |\chi_{zxx}^{(2)}(1-r)^2 \cos^2 \theta + \chi_{zzz}^{(2)}(1+r)^2 \sin^2 \theta|^2 \quad (\text{S16})$$

We highlight **reflection-induced terms in magenta** and **ϕ -dependent terms in cyan** throughout the rest of the derivation for clarity. The objective collects both components I_x and I_z in the plane of incidence; thus, the detected light has the intensity I_p :

$$I_p = I_x \cos^2 \theta + I_z \sin^2 \theta \quad (\text{S17})$$

Inserting **S14** and **S16** into **S17**, we obtain:

$$I_p \propto |\chi_{xxz}^{(2)} \cdot 2 \sin \theta \cos^2 \theta (1-r)(1+r) + \chi_{yyy}^{(2)} \cos^3 \theta (1-r)^2 \sin 3\phi|^2 + |\chi_{zxx}^{(2)} \sin \theta \cos^2 \theta (1-r)^2 + \chi_{zzz}^{(2)} \sin^3 \theta (1+r)^2|^2 \quad (\text{S18})$$

This expression holds for a specific angle θ . However, the objective accepts light of all angles between 0 and $\arcsin(\text{NA})$, where $\text{NA} = 0.75$ is the numerical aperture. Therefore, we integrate I_p over this angle range to obtain the measured I_p :

$$I_p \propto \int_0^{\arcsin(\text{NA})} \underbrace{(|\chi_{zxx}^{(2)} q_1 + \chi_{zzz}^{(2)} q_2|^2)}_{\rightarrow \mathbb{A}} + \underbrace{|\chi_{xxz}^{(2)} q_3 + \chi_{yyy}^{(2)} q_4 \sin 3\phi|^2}_{\rightarrow \mathbb{B}} d\theta \quad (\text{S19})$$

Here, we introduce θ -dependent expressions $q_{1,2,3,4}$ for readability, highlighted in **green**:

$$q_1 = \sin \theta \cos^2 \theta (1-r)^2 \quad (\text{S20})$$

$$q_2 = \sin^3 \theta (1+r)^2 \quad (\text{S21})$$

$$q_3 = 2 \sin \theta \cos^2 \theta (1-r)(1+r) \quad (\text{S22})$$

$$q_4 = \cos^3 \theta (1-r)^2 \quad (\text{S23})$$

We further develop integrals \mathbb{A} and \mathbb{B} , where we implicitly use integration boundaries as defined in **S19**:

$$\begin{aligned} \mathbb{A} &= \int |\chi_{zxx}^{(2)} q_1 + \chi_{zzz}^{(2)} q_2|^2 d\theta = \int (\chi_{zxx}^{(2)} q_1 + \chi_{zzz}^{(2)} q_2)(\chi_{zxx}^{(2)} q_1^* + \chi_{zzz}^{(2)} q_2^*) d\theta \\ &= \int (|\chi_{zxx}^{(2)}|^2 q_1 q_1^* + |\chi_{zzz}^{(2)}|^2 q_2 q_2^* + \chi_{zxx}^{(2)} \chi_{zzz}^{(2)} (q_1^* q_2 + q_1 q_2^*)) d\theta \\ &= \mathcal{I}_{11} |\chi_{zxx}^{(2)}|^2 + \mathcal{I}_{22} |\chi_{zzz}^{(2)}|^2 + \mathcal{I}_{12} \chi_{zxx}^{(2)} \chi_{zzz}^{(2)} \end{aligned} \quad (\text{S24})$$

$$\begin{aligned} \mathbb{B} &= \int |\chi_{xxz}^{(2)} q_3 + \chi_{yyy}^{(2)} q_4 \sin 3\phi|^2 d\theta = \int (\chi_{xxz}^{(2)} q_3 + \chi_{yyy}^{(2)} q_4 \sin 3\phi)(\chi_{xxz}^{(2)} q_3^* + \chi_{yyy}^{(2)} q_4^* \sin 3\phi) d\theta \\ &= \int (|\chi_{xxz}^{(2)}|^2 q_3 q_3^* + |\chi_{yyy}^{(2)}|^2 q_4 q_4^* \sin^2 3\phi + \chi_{xxz}^{(2)} \chi_{yyy}^{(2)} (q_3 q_4^* + q_3^* q_4) \sin 3\phi) d\theta \\ &= \mathcal{I}_{33} |\chi_{xxz}^{(2)}|^2 + \mathcal{I}_{44} |\chi_{yyy}^{(2)}|^2 \sin^2 3\phi + \mathcal{I}_{34} \chi_{xxz}^{(2)} \chi_{yyy}^{(2)} \sin 3\phi \end{aligned} \quad (\text{S25})$$

Here, we introduce the following integrals in **orange** which we later evaluate numerically:

$$\mathcal{I}_{11} = \int q_1 q_1^* d\theta = \int \sin^2 \theta \cos^4 \theta (1-r)^2 (1-r^*)^2 d\theta \quad (\text{S26})$$

$$\mathcal{I}_{22} = \int q_2 q_2^* d\theta = \int \sin^6 \theta (1+r)^2 (1+r^*)^2 d\theta \quad (\text{S27})$$

$$\mathcal{I}_{12} = \int (q_1 q_2^* + q_1^* q_2) d\theta = \int \sin^4 \theta \cos^2 \theta ((1-r)^2 (1+r^*)^2 + (1-r^*)^2 (1+r)^2) d\theta \quad (\text{S28})$$

$$\mathcal{I}_{33} = \int q_3 q_3^* d\theta = \int 4 \sin^2 \theta \cos^4 \theta (1-r^2) (1-r^{*2}) d\theta \quad (\text{S29})$$

$$\mathcal{I}_{44} = \int q_4 q_4^* d\theta = \int \cos^6 \theta (1-r)^2 (1-r^*)^2 d\theta \quad (\text{S30})$$

$$\mathcal{I}_{34} = \int (q_3 q_4^* + q_3^* q_4) d\theta = \int 2 \sin \theta \cos^5 \theta ((1-r^2) (1-r^*)^2 + (1-r^{*2}) (1-r)^2) d\theta \quad (\text{S31})$$

Using the above defined integrals, we can rewrite Eq. S19 as:

$$I_p \propto \mathbb{A} + \mathbb{B} = \mathcal{I}_{11} |\chi_{zxx}^{(2)}|^2 + \mathcal{I}_{22} |\chi_{zzz}^{(2)}|^2 + \mathcal{I}_{12} \chi_{zxx}^{(2)} \chi_{zzz}^{(2)} + \mathcal{I}_{33} |\chi_{xxz}^{(2)}|^2 + \mathcal{I}_{44} |\chi_{yyy}^{(2)}|^2 \sin^2 3\phi + \mathcal{I}_{34} \chi_{xxz}^{(2)} \chi_{yyy}^{(2)} \sin 3\phi \quad (\text{S32})$$

As discussed in the main text, to give a quantitative estimate of the out-of-plane components compared to the in-plane components, we reduce the number of unknown parameters in Eq. S32, and thus, simplify the $\chi^{(2)}$ tensor by applying the Kleinman's symmetry to obtain $\chi_{xxz}^{(2)} = \chi_{zxx}^{(2)}$ [8, 9]. While in ref. [8] $\chi_{zzz}^{(2)}$ was neglected, we use a more reasonable estimate consulting theory [7] to further reduce the parameter space by expressing $\chi_{zzz}^{(2)}$ in terms of $\chi_{xxz}^{(2)}$, where $\chi_{xxz}^{(2)}/\chi_{zzz}^{(2)} \approx 4$. Finally, we come to the final expression containing only parameters \mathbb{P}_1 and \mathbb{P}_2 :

$$I_p \propto \left(\mathcal{I}_{11} + \frac{1}{16} \mathcal{I}_{22} + \frac{1}{4} \mathcal{I}_{12} + \mathcal{I}_{33} \right) \underbrace{|\chi_{xxz}^{(2)}|^2}_{\mathbb{P}_1} + \mathcal{I}_{34} \underbrace{\chi_{xxz}^{(2)}}_{\mathbb{P}_1} \underbrace{\chi_{yyy}^{(2)}}_{\mathbb{P}_2} \sin 3\phi + \mathcal{I}_{44} \underbrace{|\chi_{yyy}^{(2)}|^2}_{\mathbb{P}_2} \sin^2 3\phi \quad (\text{S33})$$

We calculate the integrals numerically to obtain the following values:

$$\mathcal{I}_{11} = 0.1201, \mathcal{I}_{22} = 0.1161, \mathcal{I}_{12} = -0.1016, \mathcal{I}_{33} = 0.5924, \mathcal{I}_{44} = 1.1631, \mathcal{I}_{34} = 0.5002. \quad (\text{S34})$$

Finally, by fitting the data in Figure 3 in the main text using S33 and relative weighting, we extract the parameters \mathbb{P}_1 and \mathbb{P}_2 , and thus, obtain the ratio $\mathbb{P}_2/\mathbb{P}_1 = \chi_{yyy}^{(2)}/\chi_{xxz}^{(2)} = 8.4$.

POLARIZATION-RESOLVED SHG: MoSSe AND MoS₂

To obtain polarization-resolved SHG intensity data, we first subtract the instrumentation noise (dark counts), shown in Figure S3a and S3b in gray. To eliminate the influence of potential setup-induced polarization distortions, we compare well-studied MoS₂ monolayer to MoSSe Janus monolayer response, while keeping the same laser wavelength and power. For both materials, excitation is far from the exciton resonances to avoid unwanted TP-PL signal. Figure S3b shows that the minimum detected SHG intensity of MoSSe Janus monolayer is well above the noise level, in contrast to the signal from MoS₂ monolayer which shows minima within the noise band as presented in S3a. Figure S3c shows noise-corrected normalized SHG intensity of MoS₂, reaching minima one order of magnitude smaller than MoSSe Janus monolayer in Figure S3d.

SHG IMAGING OF MoSSe AND WSSe JANUS MONOLAYERS

Figure S4a (S4c) presents a spatial map of integrated SHG intensity revealing a prototypical MoSSe (WSSe) Janus monolayer flake with a micrograph in the bottom left (scale bar is 10 μm). Figure S4b (S4d) outlines the MoSSe (WSSe) Janus monolayer crystal orientation extracted from polarization-dependent SHG measurement, revealing zig-zag and armchair crystal directions.

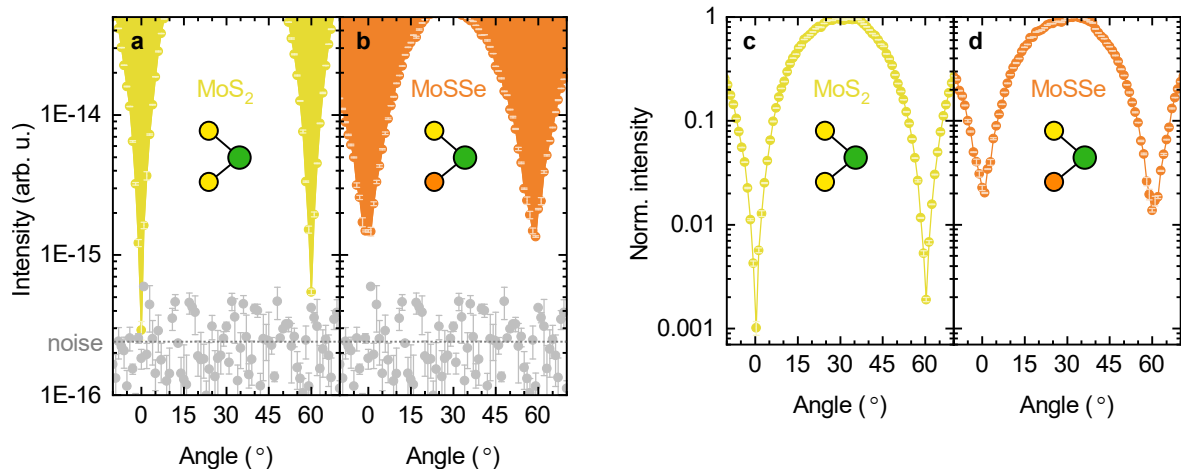


Figure S3. Polarization-resolved SHG intensity of MoSSe Janus monolayer and MoS₂ monolayer (a,b) Absolute intensity of polarization-resolved SHG of (a) MoS₂ (yellow) and (b) MoSSe Janus (orange) monolayer compared to the APD dark counts. (c,d) Logarithmic plots of the normalized polarization-resolved SHG intensity of (c) MoS₂ (yellow) and (d) MoSSe Janus (orange) monolayer. Error bars represent standard deviation obtained from multiple readouts.

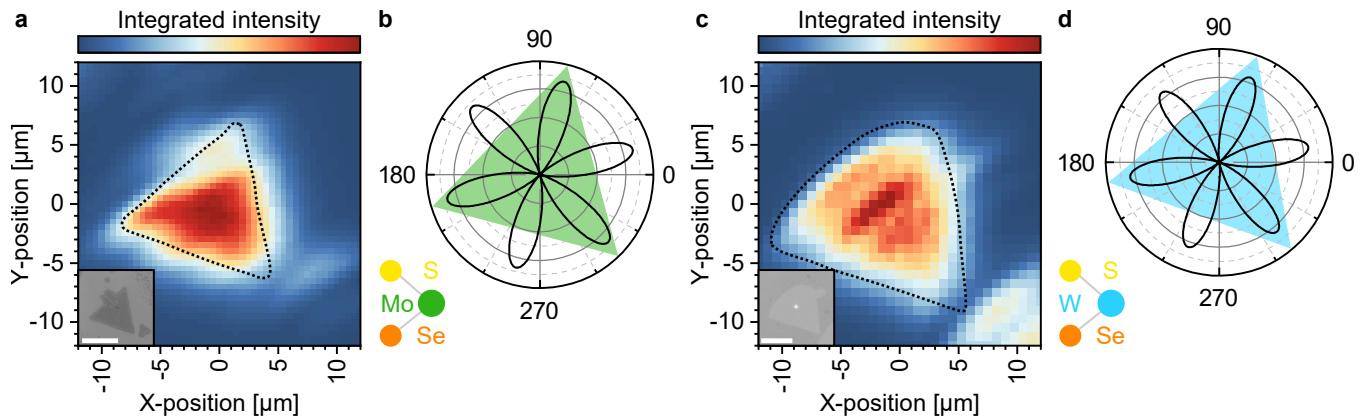


Figure S4. SHG imaging of MoSSe and WSe₂ Janus monolayer flakes. (a,c) Spatial map of integrated SHG intensity from (a) MoSSe and (c) WSe₂ Janus monolayer. Micrographs in the bottom left corner have scale bars of 10 μm . (b,d) Respective six-fold patterns reveal crystal orientation.

* Marko.Petric@wsi.tum.de

† sefaattin.tongay@asu.edu

‡ giancarlo.soavi@uni-jena.de

§ Matteo.Barbone@wsi.tum.de

- [1] N. Bloembergen, Conservation laws in nonlinear optics*, *Journal of the Optical Society of America* **70**, 1429 (1980).
- [2] J. Xiao, Z. Ye, Y. Wang, H. Zhu, Y. Wang, and X. Zhang, Nonlinear optical selection rule based on valley-exciton locking in monolayer ws₂, *Light: Science & Applications* **4**, e366 (2015).
- [3] K. L. Seyler, J. R. Schaibley, P. Gong, P. Rivera, A. M. Jones, S. Wu, J. Yan, D. G. Mandrus, W. Yao, and X. Xu, Electrical control of second-harmonic generation in a WSe₂ monolayer transistor, *Nature Nanotechnology* **10**, 407 (2015).
- [4] D. Zhang, Z. Zeng, Q. Tong, Y. Jiang, S. Chen, B. Zheng, J. Qu, F. Li, W. Zheng, F. Jiang, H. Zhao, L. Huang, K. Braun, A. J. Meixner, X. Wang, and A. Pan, Near-Unity Polarization of Valley-Dependent Second-Harmonic Generation in Stacked TMDC Layers and Heterostructures at Room Temperature, *Advanced Materials* **32**, 1908061 (2020).
- [5] R. I. Woodward, R. T. Murray, C. F. Phelan, R. E. P. de Oliveira, T. H. Runcorn, E. J. R. Kelleher, S. Li, E. C. de Oliveira, G. J. M. Fecine, G. Eda, and C. J. S. de Matos, Characterization of the second- and third-order nonlinear optical susceptibilities of monolayer MoS₂ using multiphoton microscopy, *2D Materials* **4**, 011006 (2016).

- [6] A. Autere, H. Jussila, A. Marini, J. R. M. Saavedra, Y. Dai, A. Säynätjoki, L. Karvonen, H. Yang, B. Amirsolaimani, R. A. Norwood, N. Peyghambarian, H. Lipsanen, K. Kieu, F. J. G. de Abajo, and Z. Sun, Optical harmonic generation in monolayer group-VI transition metal dichalcogenides, *Physical Review B* **98**, 115426 (2018).
- [7] N. A. Pike and R. Pachter, Angular Dependence of the Second-Order Nonlinear Optical Response in Janus Transition Metal Dichalcogenide Monolayers, *The Journal of Physical Chemistry C* **126**, 16243 (2022).
- [8] A.-Y. Lu, H. Zhu, J. Xiao, C.-P. Chuu, Y. Han, M.-H. Chiu, C.-C. Cheng, C.-W. Yang, K.-H. Wei, Y. Yang, Y. Wang, D. Sokaras, D. Nordlund, P. Yang, D. A. Muller, M.-Y. Chou, X. Zhang, and L.-J. Li, Janus monolayers of transition metal dichalcogenides, *Nature Nanotechnology* **12**, 744 (2017).
- [9] R. W. Boyd, *Nonlinear Optics*, 3rd ed. (Academic Press, Amsterdam ; Boston, 2008).